Electron Acceleration in a Dynamically Evolved Current Sheet Under Solar Coronal Conditions

Shaohua Zhang, A. M. Du, Xueshang Feng, Xin Cao, Quanming Lu, Liping Yang, Gengxiong Chen & Ying Zhang

Solar Physics

289/5

Springer

ISSN 0038-0938

Springer

Springer

Electron Acceleration in a Dynamically Evolved Current Sheet Under Solar Coronal Conditions

**Shaohua Zhang · A.M. Du · Xueshang Feng · Xin Cao ·
Quanming Lu · Liping Yang · Gengxiong Chen ·
Ying Zhang**

Abstract Electron acceleration in a drastically evolved current sheet under solar coronal
conditions is investigated via the combined 2.5-dimensional (2.5D) resistive magnetohydro-
dynamics (MHD) and test-particle approaches. Having a high magnetic Reynolds number
(10^5), the long, thin current sheet is torn into a chain of magnetic islands, which grow in
size and coalesce with each other. The acceleration of electrons is explored in three typical
evolution phases: when several large magnetic islands are formed (phase 1), two of these is-
lands are approaching each other (phase 2), and almost merging into a "monster" magnetic
island (phase 3). The results show that for all three phases electrons with an initial Maxwell
distribution evolve into a heavy-tailed distribution and more than 20 % of the electrons can
be accelerated higher than 200 keV within 0.1 second and some of them can even be ener-
gized up to MeV ranges. The lower-energy electrons are located away from the magnetic
separatrices and the higher-energy electrons are inside the magnetic islands. The most en-
ergetic electrons have a tendency to be around the outer regions of the magnetic islands or
to appear in the small secondary magnetic islands. It is the trapping effect of the magnetic
islands and the distributions of E_p that determine the acceleration and spatial distributions
of the energetic electrons.

Keywords Solar flare · Electron acceleration · Magnetic reconnection · Magnetic island ·
Parallel electric field

S. Zhang · A.M. Du (✉) · X. Cao · G. Chen · Y. Zhang
Key Laboratory of Ionospheric Environment, Institute of Geology and Geophysics, Chinese Academy
of Sciences, Beijing 100029, China
e-mail: amdu@mail.iggcas.ac.cn

S. Zhang · X. Feng
State Key Laboratory of Space Weather, Center for Space Science and Applied Research, Chinese
Academy of Sciences, Beijing 100190, China

Q. Lu
School of Earth and Space Sciences, University of Science and Technology of China, Hefei, Anhui,
China

L. Yang
School of Earth and Space Sciences, Peking University, Beijing, China

1. Introduction

Electron acceleration is one of the fundamental problems to be solved in solar-flare theories, and it is widely recognized that magnetic reconnection plays an important role in generating energetic electrons (Aschwanden, 2002; Birn and Priest, 2007; Zweibel and Yamada, 2009). The process of electron acceleration is intimately related to energy release. Through magnetic reconnection, the energy previously stored in the magnetic fields can be efficiently released, and thus converted into the bulk acceleration of electrons. Radio and hard X-ray observations indicate that the accelerated electrons with energies of tens of keV to several MeV carry a large fraction of the energy released during the impulsive phases of flares (Bastian, Benz, and Gary, 1998; Aschwanden, 2002). Yet the precise electron-acceleration mechanism in flare-associated magnetic-reconnection processes is still less well understood (Lin, 2011; Zharkova *et al.*, 2011).

Recent results from both observations and simulations suggest that magnetic islands (or plasmoids) formed during the magnetic-reconnection process are of critical importance for electron acceleration. Island coalescence also presents a potential new mechanism for electron acceleration during reconnection.

In the solar corona, magnetic-island-like structures (or plasma blobs) and the related electron-acceleration signal are often observed. The moving blob-like features observed in soft X-ray and EUV ranges above flare-loops are often interpreted as signatures of plasmoids formed in the flare-associated reconnection process due to current-sheet tearing (Bárta, Vršnak, and Karlický, 2008; Nishizuka *et al.*, 2010; Karlický and Bárta, 2011). Observations showed that the magnetic coalescence can also occur at solar flares, leading to the observed radio signals (Karlický and Bárta, 2011). Takasao *et al.* (2012) found that the plasma blobs in the current-sheet structure collided with each other before they were ejected. Song *et al.* (2012) reported the first observation of macroscopic magnetic islands' coalescence and the associated electron acceleration that occurred along the current sheet behind a CME eruption. There is also observational evidence showing that the production of energetic electrons is linked to magnetic islands during reconnection in the Earth's magnetosphere (Chen *et al.*, 2008). Wang *et al.* (2010a, 2010b) reported an *in-situ* observation of energetic electrons associated with a secondary magnetic island in an ion-diffusion region using *Cluster* data.

So far, many numerical simulations have been carried out to study the formation and dynamic evolution of magnetic islands and the corresponding electron acceleration (Biskamp and Welter, 1980; Loureiro, Schekochihin, and Cowley, 2007; Samtaney *et al.*, 2009; Huang and Bhattacharjee, 2010; Loureiro *et al.*, 2012; Huang, Bhattacharjee, and Sullivan, 2011b; Shen, Lin, and Murphy, 2011; Bárta *et al.*, 2011a; Huang *et al.*, 2011; Markidis *et al.*, 2012). A chain of small magnetic islands can always be produced in a long thin current sheet because of plasmoid instability (Loureiro, Schekochihin, and Cowley, 2007). These newborn islands are dynamically evolving. They can coalesce with each other and produce much larger islands (Finn and Kaw, 1977). Theoretically this process can provide favorable conditions for electron energization (Daughton and Roytershteyn, 2011; Cassak and Shay, 2011; Baalrud *et al.*, 2011; Takasao *et al.*, 2012). Drake *et al.* (2006) found that electrons can be efficiently accelerated in contracting magnetic islands, which may be volume-filling. Pritchett (2008) pointed out that multiple islands with the guide field can produce relativistic electrons due to multiple encounters with the accelerating potentials in each single island. Tanaka *et al.* (2010) investigated the coalescence of magnetic islands, which can also lead to efficient energization of electrons. Oka *et al.* (2010a) showed that secondary islands embedded in the current sheet can even accelerate electrons more efficiently.

Electron acceleration in magnetic reconnection has been investigated previously using analytical method (Litvinenko, 1996, 2006). Recently, test-particle simulations in different magnetic- and electric-field configurations have been widely applied to investigate particle-acceleration processes (Ambrosiano *et al.*, 1988; Kliem, 1994; Nodes *et al.*, 2003; Zharkova and Gordovskyy, 2004; Gordovskyy, Browning, and Vekstein, 2010; Perri, Zimbardo, and Greco, 2011; Li and Lin, 2012). Particle in cell (PIC) simulations are also used to study the detailed energization mechanism of electrons (Fu, Lu, and Wang, 2006; Tanaka *et al.*, 2010; Oka *et al.*, 2010a; Karlický and Bárta, 2011; Hoshino, 2012). Yet one of the limitations of PIC simulations is that the spatial size of the simulation domain is always less than hundreds of the ion inertial scale d_i [≈ 100 m], which is much smaller than the typical size of a current sheet in solar coronal conditions (around 10^7 m).

In this article, based on the magnetic and electric field obtained from 2.5-dimensional resistive MHD simulations, the test-particle method is employed to examine the electron-acceleration process in a dynamically evolving current sheet of solar coronal conditions. We show how electrons are accelerated by the magnetic islands formed in the impulsive and bursty magnetic reconnection. This article is organized as follows: In Section 2, the simulation model and test-particle method are briefly presented. Section 3 is dedicated to the evolution of magnetic reconnections and the acceleration and distribution of energetic electrons. The summary and discussion are reserved for the final section.

2. Simulation Model

2.1. Resistive MHD Model

The magnetic-reconnection process can be described by the resistive MHD equations in non-dimensional form as follows:

$$\partial_t \rho + \nabla \cdot \rho \mathbf{u} = 0 \tag{1}$$

$$\partial_t(\rho \mathbf{u}) + \nabla \cdot \left[\rho \mathbf{uu} + \left(p + \frac{1}{2}B^2 \right)\mathbf{I} - \mathbf{BB} \right] = 0 \tag{2}$$

$$\partial_t e + \nabla \cdot \left[\left(e + p + \frac{1}{2}B^2 \right)\mathbf{u} - (\mathbf{u} \cdot \mathbf{B})\mathbf{B} \right] = \eta \nabla \cdot \left[\mathbf{B} \times (\nabla \times \mathbf{B}) \right] \tag{3}$$

$$\partial_t \mathbf{B} - \nabla \times (\mathbf{u} \times \mathbf{B}) = \eta \nabla^2 \mathbf{B} \tag{4}$$

where ρ, $\mathbf{u}$, $\mathbf{B}$, $e(= \frac{1}{2}\rho \mathbf{u}^2 + \frac{p}{\gamma - 1} + \frac{1}{2}\mathbf{B}^2)$, and p are mass density, flow velocity, magnetic field, plasma energy, and thermal pressure, respectively. η (the magnetic resistivity) is set to be uniform, and its non-dimensional value taken in this article is 10^{-5}. γ ($= 5/3$) is the adiabatic index. The length, magnetic strength, density, velocity, and time are expressed in units of L_0, B_0, ρ_0, $V_0 = B_0/\sqrt{\mu \rho_0}$ (with μ the vacuum permittivity) and $\tau_0 = L_0/V_0$, respectively. In the simulation below, we take the characteristic values of solar coronal conditions, with mass density, magnetic-field strength, temperature, and length scale: $\rho_0 = 2.1 \times 10^{-11}$ kg m^{-3}, $B_0 = 40$ Gauss, $T_0 = 2.0 \times 10^6$ K, and $L_0 = 600$ km, respectively. Then the normalized time is $\tau_0 = 0.74$ seconds.

To solve the resistive MHD equations (1) through (4), we utilize our 2.5D adaptive mesh refinement (AMR) resistive MHD model (hereafter we refer to as AMR–KNPCT), in which the AMR technique is introduced with the benefit of the AMR package named PARAMESH (MacNeice *et al.*, 2000). Our numerical simulation is based on the HLL scheme, which is robust and efficient among various kinds of approximate Riemann solvers (Miyoshi and

Figure 1 The initial condition, in which the blue arrows point to directions of the magnetic-field lines and the thin red slab in the center is the current sheet. The yellow symbol represents the place where a perturbation is imposed.
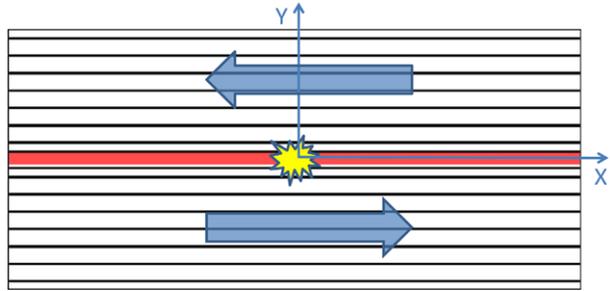
Kusano, 2005). The Constraint Transport (CT) method is used to satisfy the solenoidal condition of the magnetic field, keeping $\nabla \cdot \mathbf{B}$ close to the round-off error (Tóth, 2000; Li and Li, 2004). The TVD–MUSCL scheme enables us to achieve the second-order accuracy in space, while the Runge–Kutta method gives second-order accuracy in time. A min–mod limiter is used to suppress the numerical oscillation. This model has been used to study the magnetic-reconnection problem under real solar-wind and also solar-coronal conditions (Wang *et al.*, 2010c; Zhang *et al.*, 2011). By using the AMR technique, this code can adjust the size of the computational grid automatically in the regions where the gradients of variables (*e.g.*, the current) exceed a threshold. So, taking advantage of the AMR method, we can resolve the fine structures and at the same time can significantly save computational resources. The smallest mesh size in the y-direction is less than $0.001\,L_0$, which is sufficient for resolving the thinnest current sheets, and the simulation results tested with higher resolution are found to converge.

As shown in Figure 1, the initial condition is set up as a Harris equilibrium with a uniform guide (out-of-plane) field. The initial magnetic field is given as $\mathbf{B}_0(y) = [B_0 \tanh(y/\lambda)]\hat{\mathbf{x}}$, where λ is the half-width of the current sheet and equal to $0.5L_0$. The guide field B_z is set to $0.2B_0$. To balance the total pressure, the density is chosen as $\rho = \rho_0 \sec^2(y/\lambda) + 0.2\rho_0$. The velocity is zero. The simulation box size is $[-12.0, 12.0]L_0 \times [-4.0, 4.0]L_0$ with open boundary conditions imposed on both the x- and the y-direction. An initial flux perturbation $[\psi]$ as given by Birn *et al.* (2001) is introduced to trigger the reconnection. Here, $\psi(x, y) = \psi_0 B_0 \cos(2\pi x/L_x)\cos(\pi y/L_y)$, where the value of ψ_0 is set as 0.1, and L_x and L_y are the length and width of the simulation box, respectively.

2.2. Test-Particle Method

In typical coronal conditions, the gyro-radii for electrons are quite small (less than meter scale), so the guiding-center approximation is often employed (Gordovskyy, Browning, and Vekstein, 2010). The electron-motion equations of the relativistic guiding-center approximation are as follows:

$$\frac{\mathrm{d}\mathbf{r}}{\mathrm{d}t} = \mathbf{u}_\perp + \frac{(\gamma v_\parallel)}{\Upsilon}\mathbf{b} \tag{5}$$

$$\mathbf{u}_\perp = \mathbf{u}_E + \frac{m}{q}\frac{(\gamma v_\parallel)^2}{\Upsilon \kappa^2 B}\big[\mathbf{b}\times(\mathbf{b}\cdot\nabla)\mathbf{b}\big] + \frac{m}{q}\frac{\mu}{\Upsilon \kappa^2 B}\big[\mathbf{b}\times\nabla(\kappa B)\big]$$

$$+ \frac{m}{q}\frac{(\gamma v_\parallel)}{\kappa^2 B}\big[\mathbf{b}\times(\mathbf{b}\cdot\nabla)\mathbf{u}_E\big] + \frac{m}{q}\frac{(\gamma v_\parallel)}{\kappa^2 B}\big[\mathbf{b}\times(\mathbf{u}_E\cdot\nabla)\mathbf{b}\big]$$

$$+ \frac{m}{q}\frac{\gamma}{\kappa^2 B}\big[\mathbf{b}\times(\mathbf{u}_E\cdot\nabla)\mathbf{u}_E\big] \tag{6}$$

$$\frac{\mathrm{d}(\gamma v_\parallel)}{\mathrm{d}t} = \frac{q}{m}\mathbf{E}\cdot\mathbf{b} - \frac{\mu}{\Upsilon}\big(\mathbf{b}\cdot\nabla(\kappa B)\big) + (\gamma v_\parallel)\mathbf{u}_E\cdot\big((\mathbf{b}\cdot\nabla)\mathbf{b}\big)$$
$$+ \gamma\mathbf{u}_E\cdot\big((\mathbf{u}_E\cdot\nabla)\mathbf{b}\big) \tag{7}$$

$$\Upsilon = \sqrt{\frac{c^2 + (\gamma v_\parallel)^2 + 2\mu B}{c^2 - u^2}} \tag{8}$$

In the equations above, $\mathbf{r}$ and $\mathbf{b}$ $(= \mathbf{B}/B)$ are the vectors of electron position and magnetic-field direction. m and q are mass and charge of the electron. $\mathbf{u}_\perp$ is the velocity perpendicular to the magnetic field, which includes $\mathbf{E}\times\mathbf{B}$ drifts [$\mathbf{u}_E = \mathbf{E}\times\mathbf{b}$], curvature drifts and $\nabla\times\mathbf{B}$ drifts. $v_\parallel$ is the electron velocity parallel to the magnetic field. The relativistic factor is $\gamma = 1/\sqrt{1 - v^2/c^2}$, in which v is the absolute electron velocity and c is the speed of light. The coefficient κ is $\sqrt{1 - u_E^2/c^2}$.

In order to calculate the trajectories of electrons with Equations (5)–(8), we need the values of electric field [$\mathbf{E}$] and magnetic field [$\mathbf{B}$] experienced by electrons, which are computed from plasma velocity [$\mathbf{u}$], magnetic field [$\mathbf{B}$], and current density [$\mathbf{J} = \nabla\times\mathbf{B}$] at the mesh points by using a bi-linear interpolation method. Then $\mathbf{E}$ is calculated as $\mathbf{E} = -\mathbf{u}\times\mathbf{B} + \eta\mathbf{J}$. Here the fourth-order Runge–Kutta method is used to advance the guiding-center approximate motion equations and to calculate the trajectories of the electrons.

3. Simulation Results

3.1. Evolution of the Reconnection

We first briefly describe the dynamical evolution of the reconnection process, with particular emphasis on the coalescence of magnetic islands and the production of secondary islands.

Figure 2 displays the contour plots of plasma density [ρ] overplotted with the magnetic-field lines (white dashed lines) at different times of $t = 30$, 36, 40, 44, 48, and $52\tau_0$. In the early stages, the reconnection is dominated by the Sweet–Parker-like reconnection model triggered by the initial disturbance. This stage lasts until $t \approx 30\tau_0$, in which process the current sheet becomes thinner and longer (Figure 2(a)). Then in the later stages, a chain of small magnetic islands appears along the current sheet because of plasmoid instability (Loureiro, Schekochihin, and Cowley, 2007) when the aspect ratio of the current sheet is higher than 100. At $t = 36\tau_0$ there are eight small magnetic islands with the size of about $0.6 \times 0.15 L_0$ along the current sheet (Figure 2(b)). Three pairs of these small magnetic islands move toward each other and coalesce, producing three large magnetic islands (Figure 2(c)). These coalesced islands grow bigger with time (Figure 2(d)), with two of them again approaching each other at $t = 48\tau_0$ (Figure 2(e)) and merging into a very large one with a length of about $6.0 L_0$ and width of $2.0 L_0$ at $t = 52\tau_0$ (Figure 2(f)). This kind of extremely large island, theoretically anticipated by Uzdensky, Loureiro, and Schekochihin (2010), is also called a monster plasmoid, which offers a possible interpretation of observable abrupt events in solar flares (Loureiro *et al.*, 2012).

As noted by black arrows in Figures 2(e) and (f), the current sheet between the magnetic islands becomes thinner and unstable again to produce secondary islands embedded in the diffusion regions. The secondary islands can catch up with the islands generated before and merge with them. Finally, we see that the initial Harris current sheet evolves into a hierarchical-like structure dominated by magnetic islands. The plasma density in the
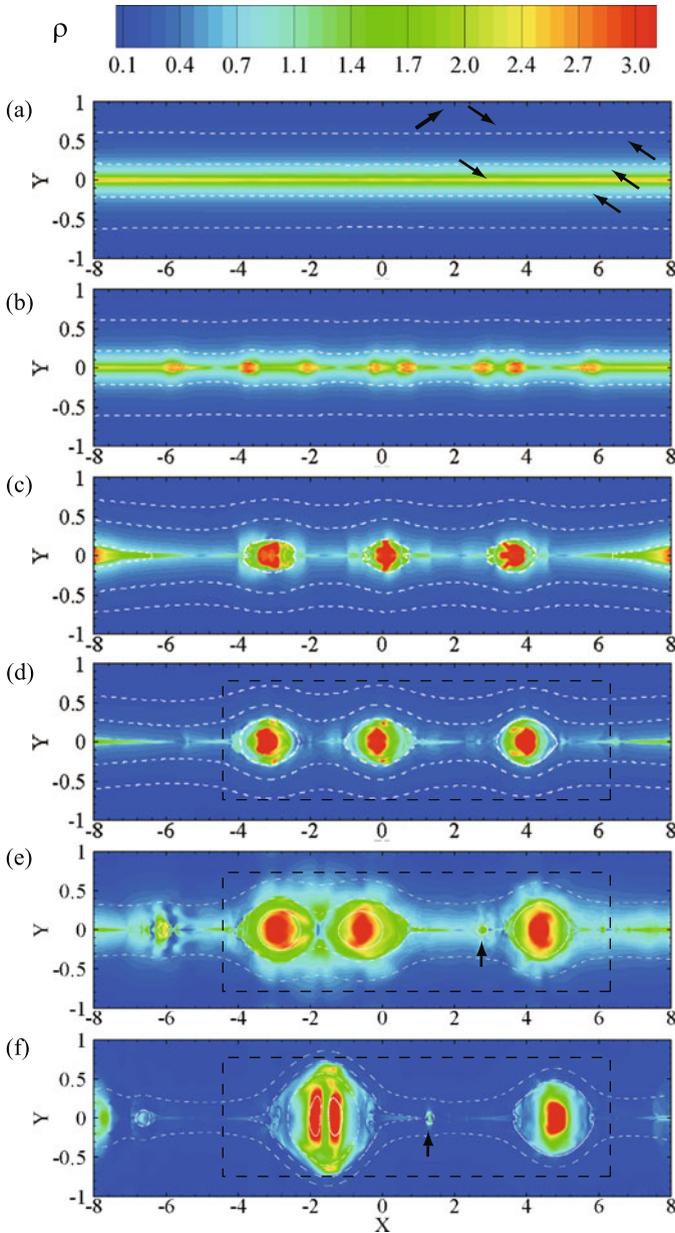
Figure 2 Plasma density [ρ] at various times for the simulation, in which the white dashed lines are the magnetic-field lines. (a) $t = 30\tau_0$, (b) $t = 36\tau_0$, (c) $t = 40\tau_0$, (d) $t = 44\tau_0$, (e) $t = 48\tau_0$, and (f) $t = 52\tau_0$. The units of the x- and of the y-axes are L_0.

magnetic islands is approximately ten times the background values. At the same time, the magnetic islands develop a relatively strong out-of-plane core magnetic field (not shown here).

Mesh resolution is critical for the simulation. If the thin current sheet is not well resolved by enough computation grids, the numerical resistivity could exceed the magnetic resistivity and anomalous numerical resistivity can be introduced, which could produce spontaneously reconnection and un-physical results. To deal with this issue, an adaptive-mesh refinement (AMR) technique is employed in the magnetic-reconnection simulation model. With the developing process of the reconnection, the model adjusts the computation grids automatically and dynamically to capture the thin current sheets. In order to validate this, Figure 3 gives the out-of-plane current [j_z] contour plot overlaid with AMR blocks and the enlarged views of the thin current sheets. Due to the AMR ability of the model, the computational blocks are automatically added to the refined thin current sheets to make sure that the current sheets are well resolved. As noted by the bold black line at $x = 1.68L_0$ in Figure 3(e), where the thinnest current sheet is located, there are about 12 grid points across the thin current sheet and the smallest mesh size in the y-direction is less than $0.001\ L_0$. We would like to point out that the analytical estimation of the dissipative current-sheet width is about $L/\sqrt{R_m} \approx 0.076L_0$, where $L = 24L_0$ is the current-sheet length and $\sqrt{R_m} = 316$. The dissipative current width $d \approx 0.03\ L_0$ (as estimated from Figure 3(e)) is pretty much in line with the analytical one as regards order of magnitude. So, the smallest resolved scale of the order of $0.001\ L_0$ is more than sufficient for the $R_m\ [= 10^5]$ considered in the simulation.

To better reveal the drastic reconnection process, Figure 4 gives a stack plot of the plasma density along the center of the current sheet ($y = 0$), from which we can see the continuous evolution of the reconnection process. The horizontal dashed lines marked by (a) – (f) correspond to the time $t = 30, 36, 40, 44, 48$, and $52\tau_0$, as shown in Figure 2. The plot illustrates that the plasma density [ρ] inside the current sheet is almost unchanged from $t = 25$ to $30\tau_0$. Then several small, high-density structures appear gradually inside the current sheet between $t = 30\tau_0$ and $t = 36\tau_0$, with each of them corresponding to a magnetic island as shown in Figure 2. As time increases, we clearly see that two high-density structures located at the left and right sides of the current sheet move out of the simulation box with the reconnection flow, whereas the other six high-density structures move toward each other and merge into three bigger structures by about $t = 36\tau_0$. The merged high-density structures grow with time, and the left two of them collide at $t = 48\tau_0$, but they still have not coalesced completely by $t = 52\tau_0$. It is interesting to see that the current sheet between these islands is unstable again due to the secondary tearing instability, which produced even much smaller islands. The black arrows shown in this figure indicate the direction of the motion of these secondary islands. Finally, some of them merge with the large islands nearby.

3.2. Results of Electron Acceleration

With the dynamic evolution of the magnetic islands, the reconnection electric field and magnetic field also developed drastically. To examine how the electrons can be accelerated by the dynamic process of the evolving magnetic islands, we choose three typical evolution phases obtained by the resistive MHD model to carry out a test-particle simulation. The three phases, respectively, start at $t = 44, 48$, and $52\tau_0$, when several large magnetic islands are formed, two of them are approaching each other and almost merging into a "monster" magnetic island (as shown in Figures 2(e), (f), and (g)). We refer to them as phase 1, phase 2, and phase 3 in the following. In each phase, based on the electric and magnetic fields generated by the resistive MHD simulation, we follow the orbits of 30 000 electrons, which are uniformly distributed in the box of $[-4.5, +6.5]\ L_0 \times [-0.8, +0.8]\ L_0$, marked by the black dashed box in Figures 2(e), (f), and (g). The initial electrons follow the Maxwell distribution and the average thermal energy is $k_B T_0 (= 172\ \text{eV})$, where k_B is the Boltzmann constant.
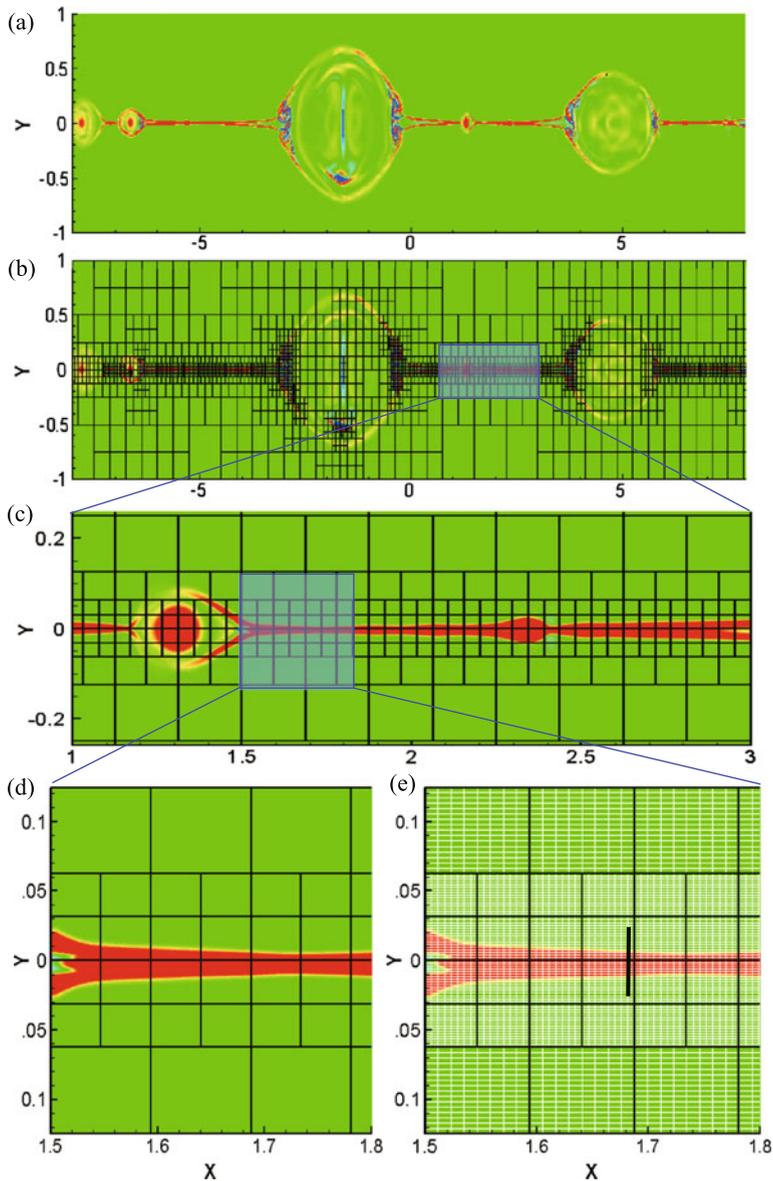
Figure 3 (a) The out-of-plane current [j_z] at $t = 52\,\tau_0$, overlaid with AMR blocks of different refinement levels (b) and the enlarged views of the thin current sheet (c), (d). Each block has 8×16 meshes, as shown in (e) by the white grids.

Figure 5 shows the electron-energy spectrum for the three phases at acceleration times of 0.0, 0.02, 0.04, and 0.10 seconds, respectively. Here, the energy E_k is defined as $E_k = (\gamma - 1)mc^2$. We can see that for all three phases, the initial Maxwellian distribution of electrons develops into a distribution of lower-energy part (with $E_k < 1.0$ keV) plus a high-energy tail (with E_k above roughly 10 keV). The lower-energy part is Maxwellian-

Figure 4 Plasma density $[\rho]$ along the current sheet ($y = 0$) as functions of time. The black arrows point to the secondary islands produced in the thinning current sheet between the islands, which eventually merge with the large islands. The units for the axes of x and t are L_0 and τ_0, respectively.
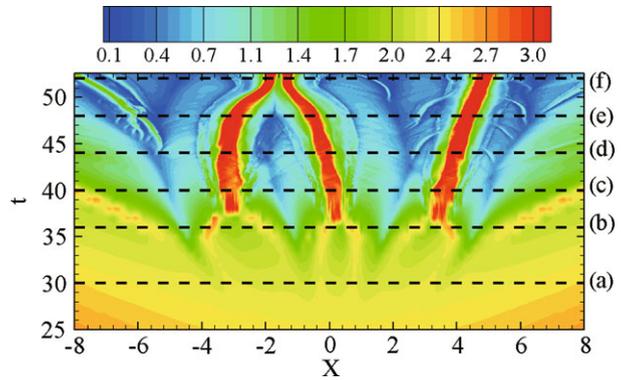
Figure 5 The energy spectrum of electrons. (a), (b), and (c) are for phase 1, phase 2, and phase 3, respectively. In each panel, the black dashed line denotes the initial distribution and the blue, green, and red lines with triangle, circle, and square symbols are the distributions at $t = 0.02$, 0.04, and 0.10 seconds, respectively, which exhibit high-energy tails and deviate strongly from the initial Maxwellians. Here, the acceleration time for electrons starts at the beginning of the respective MHD phase.
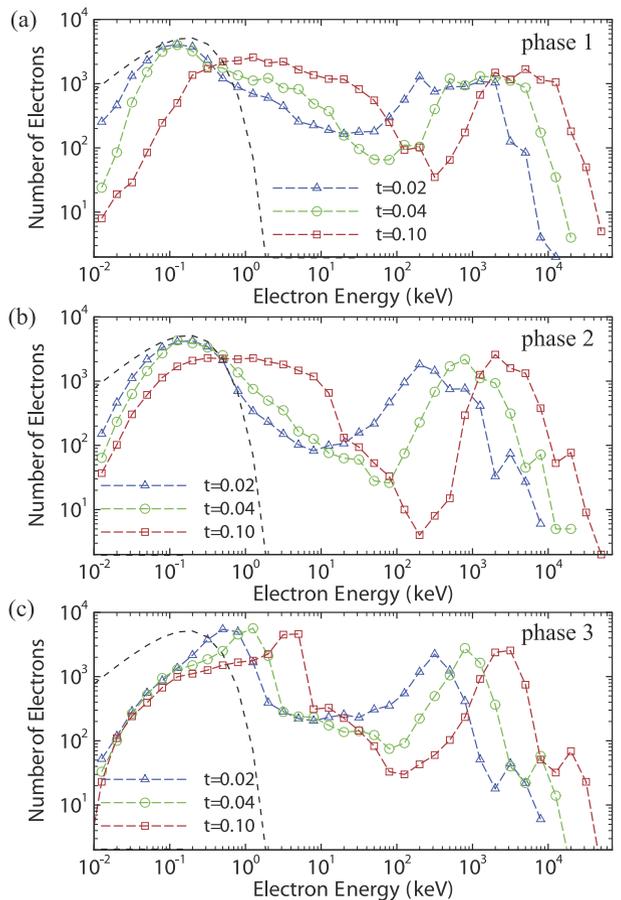
like with an overall shift toward higher energies with increasing acceleration time due to the bulk acceleration. In the high-energy tails, the electrons obtain higher and higher energies with increasing acceleration time. This can be attributed to the increased trapping time of electrons by the magnetic islands. Finally, more than 20 % of the electrons are accelerated

higher than 200 keV. It can be seen that some electrons can even be energized up to tens of MeV.

It is interesting to note that there are second higher-energy bumps at the end of high-energy tails for both phase 2 and phase 3, which do not appear in phase 1 all of the time. As shown in Figures 5(b) and (c), we will find later that the first big high-energy bump (with $E_k > 200$ keV) is affected by the large islands and the second small bump with higher energies (with E_k higher than 10 MeV) is strongly modulated by the secondary islands embedded in the diffusion region. However, in phases 1 (Figure 5(a)) there are no obvious secondary islands, so there is no second higher-energy bump.

Figures 6, 7, and 8 display the distributions of electrons at an acceleration time of 0.1 seconds for the three phases. In these figures, the top panel (a) is the energy spectrum integrated over the simulation box, in which electron energy is divided into four ranges, $E_k < 10$ keV, 10 keV $< E_k < 200$ keV, 200 keV $< E_k < 5000$ keV, and $E_k > 5000$ keV, marked by black, blue, green, and red columns, respectively. The middle three panels (b), (c), and (d) show the location of electrons projected into the $x-y$ plane for the three higher-energy ranges, which are marked by blue, green, and red square symbols, respectively. The bottom panels (e) exhibit the moving patterns of electrons, where the short lines point to the direction of motion electrons, with the magnitude scaled by $\log(E_k)$.

According to the trajectories of the electrons as shown in these figures, the energetic electrons can be sorted into two categories: One of the categories is for un-trapped electrons, moving along the open magnetic-field lines. The other type is for trapped electrons, circulating around the closed magnetic-field lines of the islands. The un-trapped electrons, most of which are out of the separatrix, have lower energies. The trapped electrons, bouncing forward and back by the magnetic islands, have much higher energies on the whole.

As shown in Figures 6(b), 7(b), and 8(b), most of the un-trapped electrons with 10 keV $< E_k < 200$ keV (marked by blue squares) are located outside the magnetic separatrices (denoted by the black dashed lines in each figure). However, almost all of the trapped electrons with 200 keV $< E_k < 5000$ keV (marked by green squares) are located inside the magnetic islands (Figures 6(c), 7(c), and 8(c)). Note that the most energetic electrons with $E_k > 5000$ keV) (marked by red squares) have a tendency to be distributed around the outer regions of the magnetic islands or at the core regions of the magnetic islands (Figures 6(d), 7(d), and 8(d)).

It can be also found that some of the most energetic electrons even appear in the small secondary magnetic islands (highlighted by the black arrows in Figures 7(d) and 8(d)), indicating that the secondary islands can accelerate electrons much more easily. In fact, Oka *et al.* (2010b) demonstrated via PIC simulations that the secondary islands embedded within the diffusion regions are efficient for producing the most energetic electrons. In the secondary island, the guide field effectively traps the electrons and keeps them in the current sheet for a long time and thus allows them to acquire more energy by the reconnection electric field (Litvinenko, 1996; Zharkova and Gordovskyy, 2004; Li and Lin, 2012).

From the moving patterns of electrons (Figures 6(e), 7(e), and 8(e)), it can be seen that the electrons mainly follow the magnetic-field lines and they are in an antiparallel direction to the in-plane magnetic-field lines. In the upper and lower half of panels (e) in each figure, the electrons with 10 keV $< E_k < 200$ keV (blue color) move toward the right and left along the in-plane magnetic-field lines, respectively. Most of the electrons with 200 keV $< E_k < 5000$ keV (green) and $E_k > 5000$ keV (red) move around the magnetic islands or secondary magnetic islands in the clockwise direction, which is in an antiparallel direction to the in-plane magnetic fields. As the electrons move along the magnetic fields, they drift
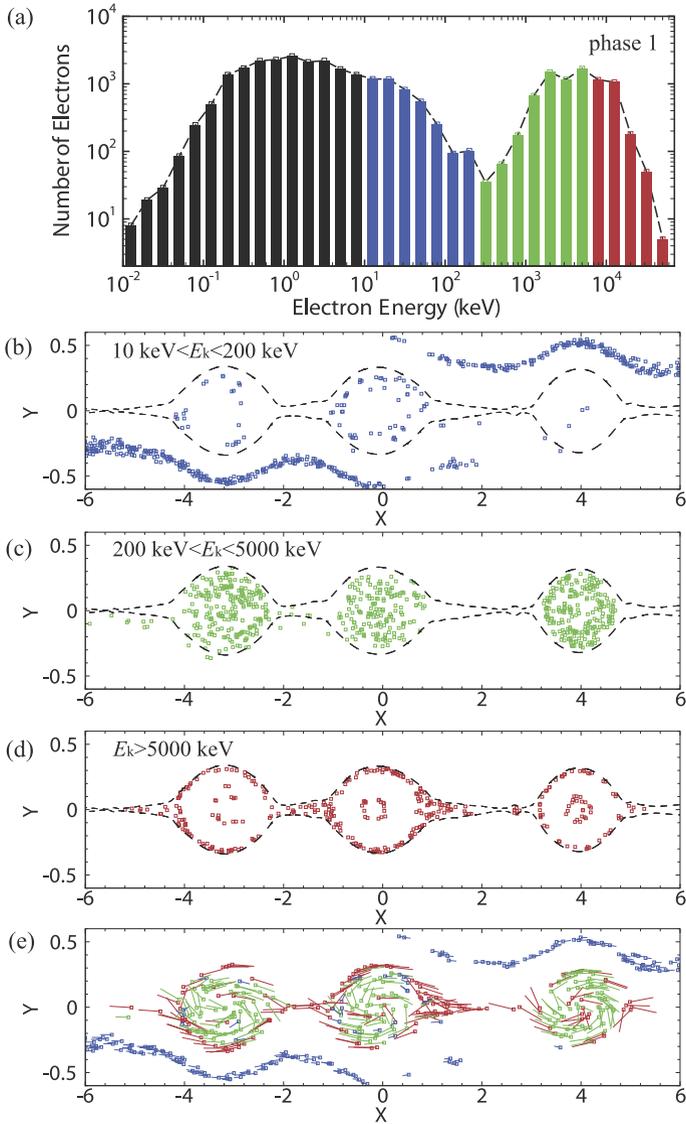
Figure 6 Phase 1: (a) Energy spectrum of electrons. (b), (c), and (d) x–y distribution of electrons with three energy ranges 10 keV < E_k < 200 keV, 200 keV < E_k < 5000 keV, and E_k > 5000 keV, marked by blue, green, and red squares, respectively. (e) The moving pattern of electrons, where the lines point to the electrons' direction of motion with the length proportional to $\log(E_k)$. Only some of the electrons are plotted to avoid clutter.

along the out-of-plane direction quickly (not shown here). The drifting distance along the out-of-plane direction is larger for the electrons in the core regions of the magnetic islands (around $40L_0$) than for those located in the edges of the magnetic islands (about $20L_0$). In fact, the directions of motion of the accelerated electrons depend on the sign of magnetic helicity in the plasmoids. It is because plasmoids are in fact flux tubes, which project onto
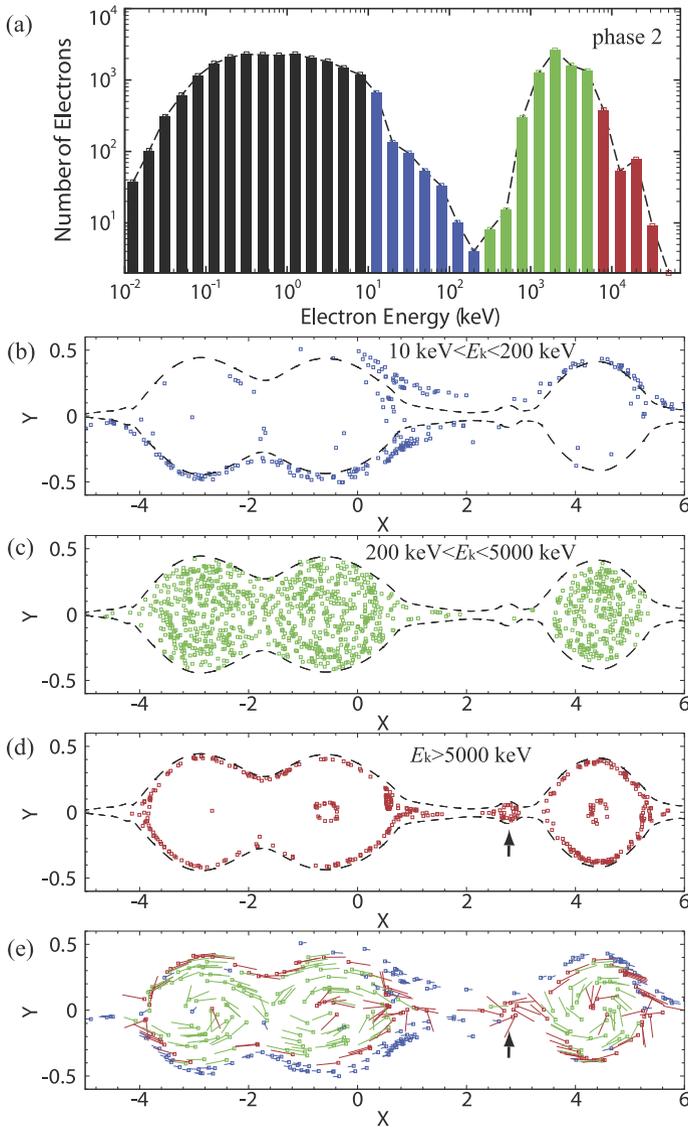
Figure 7 Phase 2: (a) Energy spectrum of electrons. (b), (c), and (d) x–y distribution of electrons with three energy ranges 10 keV $< E_k <$ 200 keV, 200 keV $< E_k <$ 5000 keV, and $E_k >$ 5000 keV, marked by blue, green, and red squares, respectively. (e) The moving pattern of electrons, where the lines point to the electrons' direction of motion with the length proportional to $\log(E_k)$. Only some of the electrons are plotted to avoid clutter. The black arrows point to the secondary islands where the most energetic electrons are located.

the x–y-plane as magnetic islands. A comparison test shows that the accelerated electrons move in the direction parallel to the in-plane magnetic field, when changing the direction of the guide field with other conditions unchanged.
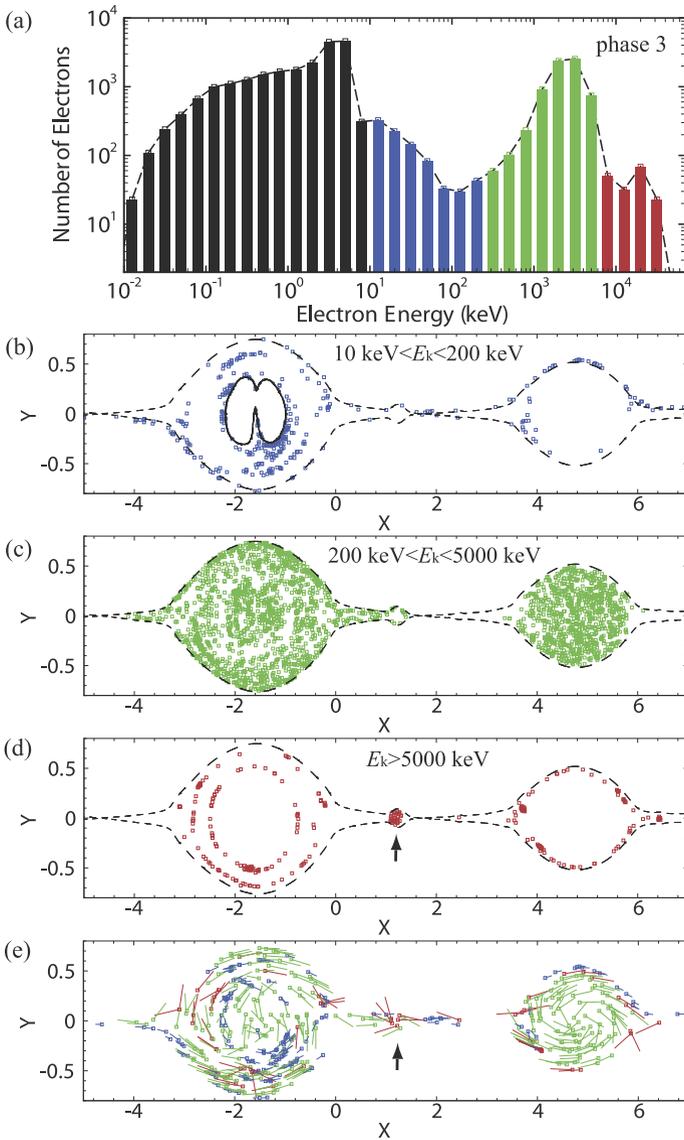
Figure 8 Phase 3: (a) Energy spectrum of electrons. (b), (c), and (d) $x-y$ distribution of electrons with three energy ranges 10 keV $< E_k <$ 200 keV, 200 keV $< E_k <$ 5000 keV, and $E_k >$ 5000 keV, marked by blue, green, and red squares, respectively. (e) The moving pattern of electrons, where the lines point to the electrons' direction of motion with the length proportional to $\log(E_k)$. Only some of the electrons are plotted to avoid clutter. The black arrows point to the secondary islands where the most energetic electrons are located.

What causes the distribution patterns of the energetic electrons? Figure 9 shows the contour plots of the parallel electric field [$E_p = \mathbf{E} \cdot \mathbf{B}/B$] for the three phases. The black dashed lines in each panel denote the magnetic-field lines.
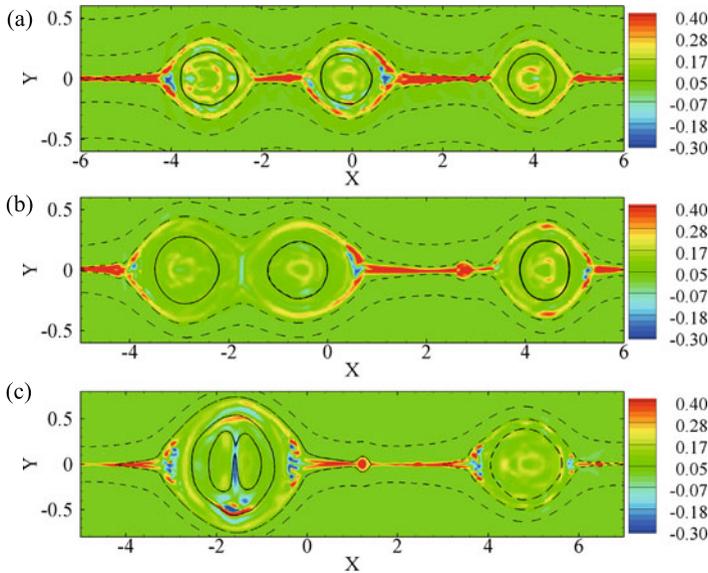
Figure 9 The contour plots of the parallel electric field $[E_\mathrm{p}]$ (volt m^{-1}) for phase 1, phase 2, and phase 3. (a) $t = 44\tau_0$, (b) $t = 48\tau_0$, and (c) $t = 52\tau_0$.

As shown in Figure 9, E_p away from the separatrix is small, so very little electron acceleration takes place in these regions. The large E_p (more than 0.1 volt m^{-1}) mainly concentrates near the X-lines and around the outer regions of the magnetic islands. Therefore, only the electrons happening to be trapped by the magnetic islands and moving along the magnetic field around the outer regions of the islands can be efficiently accelerated by the strong E_p. The electrons suddenly experience the largest acceleration kicks due to E_p enhancement. E_p in the secondary magnetic islands is large too. Therefore, the electrons trapped by the secondary magnetic islands can also be accelerated efficiently. Although the magnetic field does not accelerate the electrons directly, it influences the trajectories of electrons. So the structures of magnetic fields and E_p work together to determine the acceleration and distribution of the energetic electrons.

4. Summary and Discussion

In this study, by using a combined 2.5D resistive MHD and test-particle method, we investigate the electron acceleration by magnetic islands of various stages formed in the reconnection process of a long-thin current in the solar corona. Due to plasmoid instability, the initial current sheet breaks up into a chain of magnetic islands, which grow bigger with time and also continuously coalesce with each other. Three typical evolution phases of the resistive MHD model are chosen for test-particle simulations, using up to 30 000 electrons for each phase.

The results show that for all three phases, high-energy tails exist in all energy spectra and about 20 % of the initial electrons can be accelerated to hundreds of keV ranges in sub-second time scales. The energy and spatial distribution of electrons are related with the structures of magnetic islands. The spatial distributions of the energetic electrons show that

the electrons with 10 keV $< E_k <$ 200 keV are located outside the magnetic separatrices, where the parallel electric field [E_p] is small. The electrons with 200 keV $< E_k <$ 5000 keV are distributed inside the magnetic islands where E_p is moderately large but has complex structures. The electrons with $E_k >$ 5000 keV are located around the outer regions of the magnetic islands or at the core regions of the magnetic islands where E_p is very large. Some of the most energetic electrons (with $E_k \approx$ 10 MeV) even appear in the small secondary magnetic islands that are embedded in the diffusion regions between the magnetic islands. The trapping effect of the magnetic islands and the strong E_p around the magnetic islands or inside the secondary magnetic islands play a critical role in the acceleration process of electrons.

The discovery of radio signatures in solar flares suggests that the reconnection process in a solar flare is quasi-periodic and drastic (Kliem, Karlický, and Benz, 2000). Liu *et al.* (2010) verified the existence of a vertical current sheet above the flare loop-top in the standard CSHKP flare model and the accompanying radio pulsations implied that the current sheet must be fragmented at smaller, unresolved scales. Successive merging of plasmoids and fragmentation of flare-associated current sheets has been numerically investigated (Bárta, Vršnak, and Karlický, 2008; Bárta *et al.*, 2011a, 2011b). Our simulation results show that the dynamically evolved magnetic islands formed by reconnection of a current sheet can maintain the acceleration status, so that electrons can be very efficiently accelerated. This may provide an acceleration mechanism to explain the high-energy electrons that can produce soft/hard X-rays in solar flares.

However, the simulation in this article is 2.5D and the drifting distance for electrons is not limited in the out-of-plane direction. In the real 3D picture, magnetic islands become flux ropes which may be open-ended, so the electrons cannot be trapped inside the islands forever. In addition, the feedback effect of the electrons on the MHD simulation is ignored, and we need to incorporate the electrodynamic feedback of the accelerated electrons to the environment in which they are accelerated. These issues will be considered in our future work.

References

Ambrosiano, J., Matthaeus, W.H., Goldstein, M.L., Plante, D.: 1988, *J. Geophys. Res.* **93**, 14383. doi:10.1029/JA093iA12p14383.

Aschwanden, M.J.: 2002, *Space Sci. Rev.* **101**, 1. doi:10.1023/A:1019712124366.

Baalrud, S.D., Bhattacharjee, A., Huang, Y.M., Germaschewski, K.: 2011, *Phys. Plasmas* **18**(9), 092108. doi:10.1063/1.3633473.

Bárta, M., Vršnak, B., Karlický, M.: 2008, *Astron. Astrophys.* **477**, 649. doi:10.1051/0004-6361:20078266.

Bárta, M., Büchner, J., Karlický, M., Skála, J.: 2011a, *Astrophys. J.* **737**, 24. doi:10.1088/0004-637X/737/1/24.

Bárta, M., Büchner, J., Karlický, M., Kotrč, P.: 2011b, *Astrophys. J.* **730**, 47. doi:10.1088/0004-637X/730/1/47.

Bastian, T.S., Benz, A.O., Gary, D.E.: 1998, *Annu. Rev. Astron. Astrophys.* **36**, 131. doi:10.1146/annurev.astro.36.1.131.

Birn, J., Priest, E.R.: 2007, *Reconnection of Magnetic Fields: Magnetohydrodynamics and Collisionless Theory and Observations*. Cambridge University Press, Cambridge.

Birn, J., Drake, J.F., Shay, M.A., Rogers, B.N., Denton, R.E., Hesse, M., Kuznetsova, M., Ma, Z.W., Bhattacharjee, A., Otto, A., Pritchett, P.L.: 2001, *J. Geophys. Res.* **106**, 3715. doi:10.1029/1999JA900449.

Biskamp, D., Welter, H.: 1980, *Phys. Rev. Lett.* **44**, 1069. doi:10.1103/PhysRevLett.44.1069.

Cassak, P.A., Shay, M.A.: 2011, *Space Sci. Rev.* 265. doi:10.1007/s11214-011-9755-2.

Chen, L.J., Bhattacharjee, A., Puhl-Quinn, P.A., Yang, H., Bessho, N., Imada, S., Mühlbachler, S., Daly, P.W., Lefebvre, B., Khotyaintsev, Y., Vaivads, A., Fazakerley, A., Georgescu, E.: 2008, *Nat. Phys.* **4**, 19. doi:10.1038/nphys777.

Daughton, W., Roytershteyn, V.: 2011, *Space Sci. Rev.* 1. doi:10.1007/s11214-011-9766-z.

Drake, J.F., Swisdak, M., Che, H., Shay, M.A.: 2006, *Nature* **443**, 553. doi:10.1038/nature05116.

Finn, J.M., Kaw, P.K.: 1977, *Phys. Fluids* **20**, 72. doi:10.1063/1.861709.

Fu, X.R., Lu, Q.M., Wang, S.: 2006, *Phys. Plasmas* **13**(1), 012309. doi:10.1063/1.2164808.

Gordovskyy, M., Browning, P.K., Vekstein, G.E.: 2010, *Astrophys. J.* **720**, 1603. doi:10.1088/0004-637X/720/2/1603.

Hoshino, M.: 2012, *Phys. Rev. Lett.* **108**, 135003. doi:10.1103/PhysRevLett.108.135003.

Huang, Y.M., Bhattacharjee, A.: 2010, *Phys. Plasmas* **17**(6), 062104. doi:10.1063/1.3420208.

Huang, Y.M., Bhattacharjee, A., Sullivan, B.P.: 2011, *Phys. Plasmas* **18**(7), 072109. doi:10.1063/1.3606363.

Huang, C., Lu, Q., Yang, Z., Wu, M., Dong, Q., Wang, S.: 2011, *Nonlinear Process. Geophys.* **18**, 727. doi:10.5194/npg-18-727-2011.

Karlický, M., Bárta, M.: 2011, *Astrophys. J.* **733**, 107. doi:10.1088/0004-637X/733/2/107.

Kliem, B.: 1994, *Astrophys. J. Suppl. Ser.* **90**, 719. doi:10.1086/191896.

Kliem, B., Karlický, M., Benz, A.O.: 2000, *Astron. Astrophys.* **360**, 715.

Li, S., Li, H.: 2004, *J. Comput. Phys.* **199**, 1. doi:10.1016/j.jcp.2004.01.027.

Li, Y., Lin, J.: 2012, *Solar Phys.* **279**, 91. doi:10.1007/s11207-012-9956-1.

Lin, R.P.: 2011, *Space Sci. Rev.* **159**, 421. doi:10.1007/s11214-011-9801-0.

Litvinenko, Y.E.: 1996, *Astrophys. J.* **462**, 997. doi:10.1086/177213.

Litvinenko, Y.E.: 2006, *Astron. Astrophys.* **452**, 1069. doi:10.1051/0004-6361:20054324.

Liu, R., Lee, J., Wang, T., Stenborg, G., Liu, C., Wang, H.: 2010, *Astrophys. J. Lett.* **723**, L28. doi:10.1088/2041-8205/723/1/L28.

Loureiro, N.F., Schekochihin, A.A., Cowley, S.C.: 2007, *Phys. Plasmas* **14**(10), 100703. doi:10.1063/1.2783986.

Loureiro, N.F., Samtaney, R., Schekochihin, A.A., Uzdensky, D.A.: 2012, *Phys. Plasmas* **19**(4), 042303. doi:10.1063/1.3703318.

MacNeice, P., Olson, K.M., Mobarry, C., de Fainchtein, R., Packer, C.: 2000, *Comput. Phys. Commun.* **126**, 330. doi:10.1016/S0010-4655(99)00501-9.

Markidis, S., Henri, P., Lapenta, G., Divin, A., Goldman, M.V., Newman, D., Eriksson, S.: 2012, *Nonlinear Process. Geophys.* **19**, 145. doi:10.5194/npg-19-145-2012.

Miyoshi, T., Kusano, K.: 2005, *J. Comput. Phys.* **208**, 315. doi:10.1016/j.jcp.2005.02.017.

Nishizuka, N., Takasaki, H., Asai, A., Shibata, K.: 2010, *Astrophys. J.* **711**, 1062. doi:10.1088/0004-637X/711/2/1062.

Nodes, C., Birk, G.T., Lesch, H., Schopper, R.: 2003, *Phys. Plasmas* **10**, 835. doi:10.1063/1.1542612.

Oka, M., Phan, T.D., Krucker, S., Fujimoto, M., Shinohara, I.: 2010a, *Astrophys. J.* **714**, 915. doi:10.1088/0004-637X/714/1/915.

Oka, M., Fujimoto, M., Shinohara, I., Phan, T.D.: 2010b, *J. Geophys. Res.* **115**, 8223. doi:10.1029/2010JA015392.

Perri, S., Zimbardo, G., Greco, A.: 2011, *J. Geophys. Res.* **116**, 5221. doi:10.1029/2010JA016328.

Pritchett, P.L.: 2008, *Phys. Plasmas* **15**(10), 102105. doi:10.1063/1.2996321.

Samtaney, R., Loureiro, N.F., Uzdensky, D.A., Schekochihin, A.A., Cowley, S.C.: 2009, *Phys. Rev. Lett.* **103**(10), 105004. doi:10.1103/PhysRevLett.103.105004.

Shen, C., Lin, J., Murphy, N.A.: 2011, *Astrophys. J.* **737**, 14. doi:10.1088/0004-637X/737/1/14.

Song, H.Q., Chen, Y., Li, G., Kong, X.L., Feng, S.W.: 2012, *Phys. Rev. X* **2**(2), 021015. doi:10.1103/PhysRevX.2.021015.

Takasao, S., Asai, A., Isobe, H., Shibata, K.: 2012, *Astrophys. J. Lett.* **745**, L6. doi:10.1088/2041-8205/745/1/L6.

Tanaka, K.G., Yumura, T., Fujimoto, M., Shinohara, I., Badman, S.V., Grocott, A.: 2010, *Phys. Plasmas* **17**(10), 102902. doi:10.1063/1.3491123.

Tóth, G.: 2000, *J. Comput. Phys.* **161**, 605. doi:10.1006/jcph.2000.6519.

Uzdensky, D.A., Loureiro, N.F., Schekochihin, A.A.: 2010, *Phys. Rev. Lett.* **105**(23), 235002. doi:10.1103/PhysRevLett.105.235002.

Wang, R., Lu, Q., Du, A., Wang, S.: 2010a, *Phys. Rev. Lett.* **104**(17), 175003. doi:10.1103/PhysRevLett.104.175003.

Wang, R., Lu, Q., Li, X., Huang, C., Wang, S.: 2010b, *J. Geophys. Res.* **115**, 11201. doi:10.1029/2010JA015473.

Wang, Y., Wei, F.S., Feng, X.S., Zhang, S.H., Zuo, P.B., Sun, T.R.: 2010c, *Phys. Rev. Lett.* **105**, 195007. doi:10.1103/PhysRevLett.105.195007.

Zhang, S.H., Feng, X.S., Wang, Y., Yang, L.P.: 2011, *Chin. Phys. Lett.* **28**(8), 089601. doi:10.1088/0256-307X/28/8/089601.

Zharkova, V.V., Gordovskyy, M.: 2004, *Astrophys. J.* **604**, 884. doi:10.1086/381966.

Zharkova, V.V., Arzner, K., Benz, A.O., Browning, P., Dauphin, C., Emslie, A.G., Fletcher, L., Kontar, E.P., Mann, G., Onofri, M., Petrosian, V., Turkmani, R., Vilmer, N., Vlahos, L.: 2011, *Space Sci. Rev.* **159**, 357. doi:10.1007/s11214-011-9803-y.

Zweibel, E.G., Yamada, M.: 2009, *Annu. Rev. Astron. Astrophys.* **47**, 291. doi:10.1146/annurev-astro-082708-101726.